Appl Phys B (2012) 106:971–978
DOI 10.1007/s00340-011-4769-8

Applied Physics B
Lasers and Optics

Low temperature cavity ring down spectroscopy with off-axis alignment: application to the A- and γ-bands of O_2 in the visible at 90 K

Y. Perez-Delgado · C.E. Manzanares

Received: 8 July 2011 / Revised version: 1 August 2011 / Published online: 11 October 2011

Abstract The cavity ring down (CRD) technique presented here involves an optical cavity attached to a cryostat. The static cell and mirrors of the optical cavity are all inside a vacuum chamber at the same temperature of the cryostat. The temperature of the cell can be changed between 77 K and 298 K. An off-axis alignment of the laser beam into the cavity is used to increase the number of resonant modes inside the cavity and improve the signal to noise ratio of the absorption bands. To demonstrate the capabilities of the low temperature CRD cell, the absorption spectra of O_2 are recorded at 90 K for the A ($\upsilon' = 0 \leftarrow \upsilon'' = 0$) and γ ($\upsilon' = 2 \leftarrow \upsilon'' = 0$) bands of the $b^1\sum_g^+ \leftarrow X^3\sum_g^-$ transition using cavity ring down spectroscopy. The optical cavity performance was tested using two variations of the CRD technique. The A-band is measured using the phase-shift cavity ring down method and the γ-band using the pulsed-laser exponential-decay method. A comparison between experimental and simulated spectra of the O_2 bands at 90 K confirms the molecular temperature measured by a sensor localized in the cell. Quantitative measurements of the individual rotational line intensities are made for the oxygen γ-band to confirm the temperature of the cell and calculate the vibrational band intensity. The application of this technique for laboratory studies of planetary atmospheres and the spectroscopy of molecular complexes is emphasized.

Y. Perez-Delgado · C.E. Manzanares (✉)
Department of Chemistry & Biochemistry, Baylor University,
101 Bagby Avenue, Baylor Sciences Building E-216, Waco,
TX 76706, USA
e-mail: Carlos_Manzanares@baylor.edu
Fax: +1-254-710-4272

1 Introduction

Cavity ring down (CRD) at low temperatures has been developed in our laboratory in order to study weak absorptions of molecules relevant to planetary atmospheres [1, 2]. With our experimental set up, CRD is performed with a variable temperature (77–297 K) cavity [3, 4]. Our cavity design is such that the complete optical cavity including the mirrors is in a vacuum chamber at the temperature of the cold head of the cryostat. Our initial experiments with the low temperature optical cavity were done with on-axis excitation using the phase-shift CRD technique [5, 6] and the exponential-decay CRD technique [7–9]. Other investigations that involve low temperature CRD experiments using a static cell have measured the collision induced absorption bands of oxygen [10, 11]. Before the introduction of the CRD technique, multiple transversal cell or White cells [12] for gases operating at low temperatures were pioneered by Herzberg [13] cooled with liquid N_2 (78 K) and 80 m path length to give spectroscopic evidence for H_2 in the atmospheres of Uranus and Neptune, Watanabe and Welsh [14], using liquid H_2 (18 K), liquid N_2 (77 K) and 13 m path length studied the collision induced absorption of H_2 and D_2 at low temperatures, Ewing and co-workers [15] using liquid nitrogen (77 K), liquid Ar (87 K) and 230 m path length showed the collision induced absorption spectrum of O_2, McKellar and co-workers [16] describe a variable temperature (80–125 K) with 165 m path length cell, and Horn and Pimentel [17] describe a variable temperature (120–300 K) and variable path length cell (60 to 2540 m) to study the absorption of constituents of Martian atmosphere. These cells have been very useful to reproduce conditions of planetary atmospheres and obtain spectroscopic constants and molecular structures of van der Waals molecules.

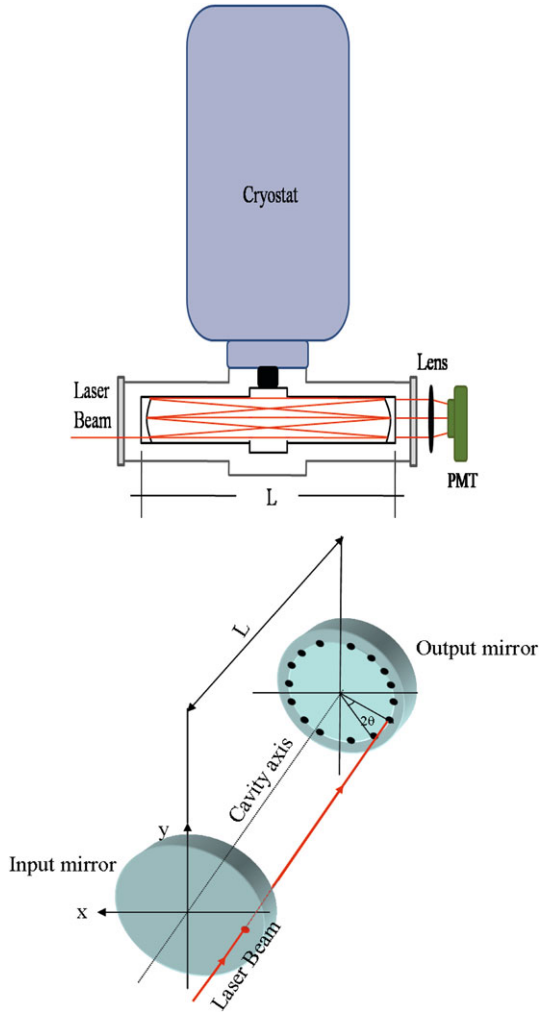

Fig. 1 (*Top*) Schematic view of the cryostat and optical cavity isolated inside a vacuum chamber. (*Bottom*) Off-axis beam propagation diagram. Predicted $\Delta\nu$ for mirrors with $r = 600$ cm and $L = 43.5$ cm of a cavity aligned on-axis ($\Delta\nu_{\text{on-axis}} = 115 \times 10^{-4}$ cm^{-1}) and off-axis ($\Delta\nu_{\text{off-axis}} = 2.8 \times 10^{-4}$ cm^{-1}) when the reentrant condition is satisfied after 41 round trips

For PS-CRD systems based on an on-axis alignment of the laser beam into the cavity, the coherent laser beam couples into the cavity on average only 5–10% of the time [6, 18]. Several methods have been used to increase the coupling-time efficiency of the laser with the cavity, improvements such as: construction of cavities with an irrational number as the ratio of cavity length to mirror curvature radius [6], using a vibrating piezoelectric material to modulate the cavity length and using laser frequency dithering [18]. When the laser beam is injected into the cavity at an angle to the optical axis (off-axis) as shown in Fig. 1, the cavity mode density increases [19] and the beam may couple into the cavity continuously up to 100% of the time [20]. Recently, it has been shown [21] that the signal to noise ratio increases in the order: on-axis < close to axis < off-axis. The off-axis laser beam cavity alignment decreases the cavity FSR and excites a large number of transverse cavity modes. The high number of excited cavity modes permits the cw laser radiation-cavity interaction to be considered as noncoherent on average [22]. Off-axis paths through optical cavities were first described by Herriot et al. [23]. The off-axis approach has been used successfully for sensitive absorption measurements in: high speed CRD detection [21], PS-Cavity enhanced absorption (CEA) [20, 24, 25], CRD spectroscopy [26, 27], and CEA spectroscopy [28–33].

In this paper, we present for the first time, the absorption spectra of the A- and γ-bands of O_2 at 90 K. Our best results were obtained with an off-axis excitation of the cavity. The off-axis PS-CRD technique is used to obtain the A-band and the off-axis pulsed CRD technique is used to obtain the γ-band. Quantitative and qualitative comparison of intensities between experimental and simulated spectra of the O_2 bands at 90 K confirms the molecular temperature measured by a sensor localized in the cell. The main objective of this research is to show the application of this technique for laboratory studies of planetary atmospheres and the spectroscopy of molecular complexes.

2 Experimental

Experimental details of our technique, cryostat, and low temperature optical cavity have been given in previous publications [1–3]. Figure 1 (top) summarizes the main components of the low temperature optical cavity. The cavity is attached to the cold head of a cryostat (International Cryogenics, model 31-4000) that can be filled with liquid N_2 or liquid He. The temperature control of the cell is achieved with an electrical heater attached to the cold head of the cryostat. The temperature is controlled with a Scientific Instruments model 9650 temperature controller and indicator. Two diode thermocouples measure simultaneously the temperature of the cold head and the cell. The entire cavity is inside a vacuum chamber fitted with quartz windows parallel to the mirrors of the cavity. A cryogenic vacuum pump (CTI cryogenics) is used to obtain a vacuum below 1×10^{-8} Torr for the chamber surrounding the cavity.

For the exponential-decay measurements we used a pulsed dye laser (Quanta-Ray PDL-3, linewidth 0.07 cm^{-1}) pumped by a Nd-YAG laser (Quanta-Ray DCR). The intensity of the light transmitted (I) out of the cavity decreases as a function of time (t). Cavity losses are due to transmission through the mirrors. The presence of absorbing species in the cavity gives an additional mechanism for loss of light from the cavity by sample absorption. In the exponential-decay experiment, the light intensity will still decay exponentially with a time dependence given by [7–9]

$$I(t) = I_0 \exp\left\{-\frac{t}{\tau} - \alpha c t\right\}, \tag{1}$$

where I_0 is the initial light intensity, α is the wavelength dependent molecular absorption coefficient with dimensions of cm^{-1}, and c is the speed of light. The product of c and τ (21.3 µs) is the path length (6.4 Km) over which the absorption was measured. Labview programs were used to control the data acquisition, laser wavelength scan, processing and displaying data. The data were acquired using a GPIB interface. Each point was the average of 30 pulses.

For the PS-CRD experiments the laser used was a Ti-Sapphire laser (Coherent 899 ring laser, linewidth 0.17 cm^{-1}) pumped by a Nd-YVO_4 laser (Coherent Verdi). The laser modulation was done with an electro-optic modulator (Conoptics 350-50). The entrance beam was an square wave of frequency 14 kHz. The scanning range was from 12500 to 14300 cm^{-1}. The PS-CRD method measures the phase-shift of a modulated beam from the output beam of the cavity with respect to the modulated beam, or reference beam, before entering the cavity. The phase-shift angle is related to the ring down time by the equation [5, 6]

$$\tan\theta = 2\pi f\tau, \tag{2}$$

where θ is the phase-shift angle and f is the modulation frequency. In this case the path length was 3.7 Km and the time constant 12.3 µs.

The decay time from the cavity filled with an absorbing gas is a combination of the sample plus the background. The inverse of the decay time of the empty cavity or background $(1/\tau_0)$ is subtracted from the inverse of the decay time of the cavity filled $(1/\tau)$ with the sample. We have

$$\alpha(\nu) = \frac{1}{c}\left[\left(\frac{1}{\tau(\nu)}\right) - \left(\frac{1}{\tau_0(\nu)}\right)\right]. \tag{3}$$

The calculated absorption ($\alpha(\nu)$ in cm^{-1} units) is plotted as a function of the wave number (cm^{-1}) to show the spectrum of the sample.

Initially the on-axis configuration was tried with poor results related to reproducibility and signal to noise ratio of the signals. In order to increase the density of cavity modes, the off-axis configuration was tested. Off-axis alignment resulted in reproducible signals of higher signal to noise ratio. The off-axis configuration spatially separates the multiple reflections within the cavity until the reentrant condition is fulfilled, that is, the time at which the ray begins to retrace its original path through the cavity. The spot pattern on the mirrors generally lies on an ellipse [23]. To maximize the circumference that can be fitted onto the mirror surface and thus the number of spots that can be accommodated without overlap, the elliptical form should be a circle near the edge of the mirrors [22], as shown in Fig. 1 (bottom). The angle of a round-trip rotation of the beam spot (2θ) is determined purely by the geometry of the cavity and is given by [23]:

$$\cos\theta = 1 - L/r, \tag{4}$$

where L is the mirror spacing and r is the mirrors radius of curvature. The reentrant condition is satisfied if [23]:

$$2m\theta = 2n\pi, \tag{5}$$

where m is the number of optical round-trip passes and n is a integer, and after every m round trips the ray starts to retrace its path. In many respect, the properties of the cavity, including the longitudinal mode spacing ($\Delta\nu$), become similar to one that is m times longer. The longitudinal mode spacing of a cavity aligned off-axis ($\Delta\nu_{\text{off-axis}}$) is

$$\Delta\nu_{\text{off-axis}} = \frac{c}{m2L} \tag{6}$$

where c is the speed of the light, L is the length of the cavity and m is the number of optical round-trip passes. Using (4) and (5), m was determined only by the geometrical parameters of the cavity and not by the beam alignment. For our cavity aligned off-axis, $L = 43.5$ cm and $r = 600$ cm, (5) gives $m = 41$, $n = 5$, and $\Delta\nu_{\text{off-axis}} = 2.8 \times 10^{-4}$ cm^{-1}. For $L = 43.5$ cm and $r = 100$ cm, (5) gives $m = 26$, $n = 8$, and $\Delta\nu_{\text{off-axis}} = 4.4 \times 10^{-4}$ cm^{-1}. For our cavity aligned on-axis $\Delta\nu_{\text{on-axis}} = 115 \times 10^{-4}$ cm^{-1}. The reentrant condition is satisfied after 41 round trips for $r = 600$ cm and $L = 43.5$ cm.

Off-axis alignment was used in the present research to increase the time that the coherent laser beam couples into the cavity. This change from on-axis to off-axis laser injection resulted in an improvement in detection sensitivity and at the same time an increase of the signal to noise ratio. With off-axis alignment of our cavity, frequency dithering and/or modulation of the cavity length with a vibrating piezoelectric material were not necessary. This is very important because our cavity is insulated under vacuum for low temperature experiments.

3 Results

The red atmospheric bands of molecular oxygen are due to the transition between the electronic triplet ground state $X^3\sum_g^-$ and the second singlet electronic state $b^1\sum_g^+$. Figure 2 (top) shows a potential energy diagram for two low-lying electronic states of O_2. The $(0 \leftarrow 0)$ and $(2 \leftarrow 0)$ bands are, respectively, denoted as the A- and γ-bands. The O_2 transitions are comprised of four branches, two R branches forming a head and two P branches, separated from the former by a zero gap. The corresponding transitions are indicated in Fig. 2 (bottom) using full lines. There is an ${}^RR$ branch ($\Delta J = +1$, $\Delta K = +1$), a ${}^PP$ branch ($\Delta J = -1$, $\Delta K = -1$), an ${}^RQ$ branch ($\Delta J = 0$, $\Delta K = +1$), and a ${}^PQ$ branch ($\Delta J = 0$, $\Delta K = -1$) [34, 35]. The three components of the $X^3\sum_g^-$ ground state of oxygen are assigned by F_1, F_2, and F_3, according as $J = K + 1$, $J = K$, and $J = K - 1$.

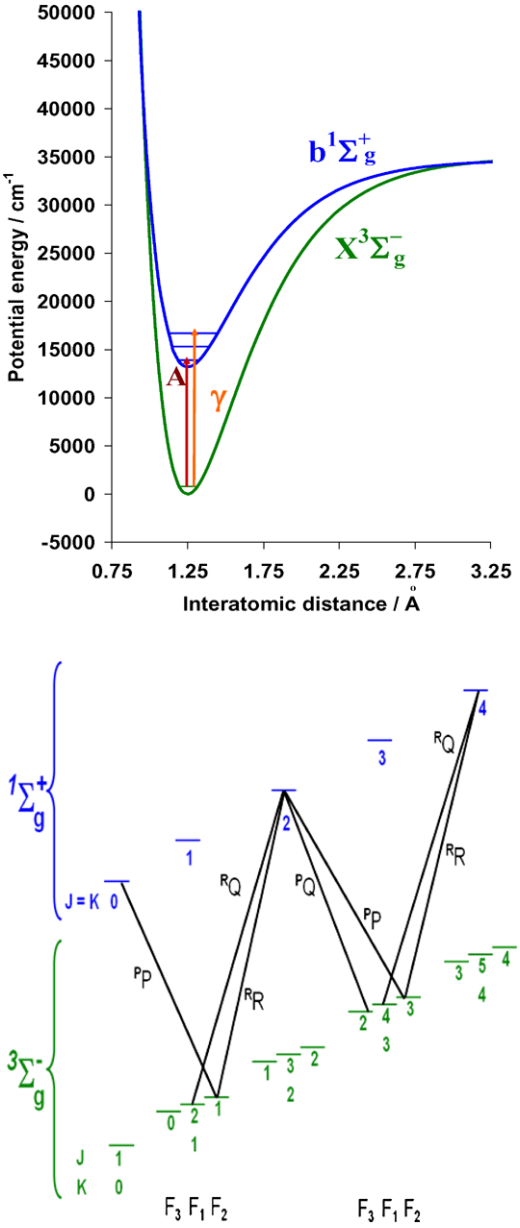

Fig. 2 (*Top*) Potential energy diagram for two electronic states of O_2. (*Bottom*) Branches of the $b^1\sum_g^+(\upsilon' = 0,2) \leftarrow X^3\sum_g^-(\upsilon'' = 0)$ bands of O_2

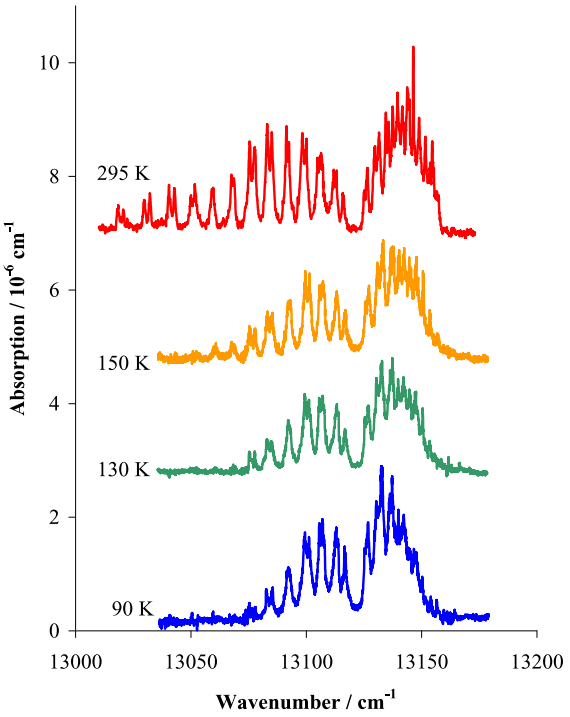

Fig. 3 Observed (PS-CRD) spectra of the oxygen A-band at four temperatures

The ^PP and ^RR branches of the red atmospheric bands correspond to transitions from the F_2 component, the ^RQ and ^PQ branches to transitions from F_1 and F_3 components, respectively. The F_i values can be calculated from equations derived by Watson [36]. Detailed equations and rotational constants were taken from the literature [37, 40]. In order to reproduce the spectra and check the accuracy of the temperature measured by the sensor in the cell, the simulated spectra at 90 K were obtained using the PGOPHER program [41]. Vibrational and rotational constants for the electronic states $X^3\sum_g^-$ and $b^1\sum_g^+$ of oxygen have been reported [42] and were used in the simulation program. The complete set of rotational equations used by the PGOPHER program as well as the rotational constants (distortion correction, spin-spin interaction, and spin-orbit interaction constants) have been reported [43–46] and were used in the calculation. The peak maximum of the calculated band was scaled to the maximum of the experimental band to facilitate the comparison between the observed and simulated bands.

Figure 3 shows the experimental spectra for the A-band of O_2 at 295, 150, 130, and 90 K.

The bands were obtained using the PS-CRD technique with the low temperature cryostat. Figure 4 shows the experimental (80 Torr) and simulated absorption spectra of the oxygen γ-band at 90 K using the pulsed CRD technique. The ^PP and ^PQ branches are better resolved in the absorption spectrum for the γ-band than the spectrum for the A-band due to the fact that the pulsed laser had a higher resolution.

The minimum absorption coefficient ($\alpha_{\min}$) that supposes a single decay uncertainty is [9]: $\alpha_{\min} = (2)^{1/2}(\delta\tau_o/c\tau_o^2)$. In our case $\delta\tau_o = 0.38$ µs, $\tau_o = 21.3$ µs, and $\alpha_{\min} = 3.95 \times 10^{-8}$ cm^{-1}. Other definitions multiply the equation by $N^{-1/2}$ ($\alpha_{\min} = 7.2 \times 10^{-9}$ cm^{-1}) with $N = 30$ averages, or multiply by $(f_{\text{rep}})^{-1/2}$ ($\alpha_{\min} = 1.25 \times 10^{-8}$ cm^{-1} Hz$^{-1/2}$) with $f_{\text{rep}} = 10$ Hz. This last one is called the noise-equivalent absorption (NEA). The lowest peak absorption that was measured in our experiment was 1.5×10^{-7} cm^{-1}. The baseline noise levels of the spectra were mainly due to

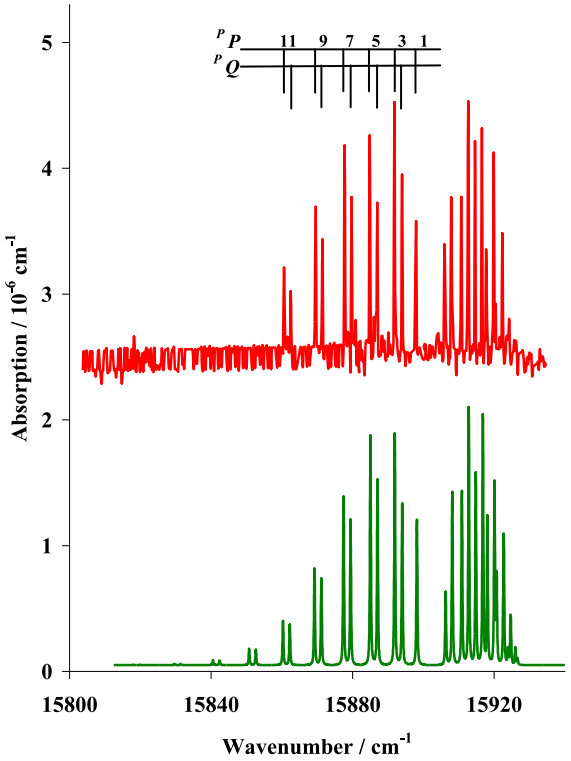

Fig. 4 Observed (CRD) and calculated absorption spectrum of 80 Torr of the oxygen γ band at 90 K

the laser used. This was an old model dye laser with low quality beam profile and jitter.

4 Discussion

The first spectroscopic study of the red system of atmospheric oxygen bands was made by Babcock and Herzberg [35] using a long path cell in the laboratory and open path measurements through the atmosphere with two different grating spectrometers. Quantitative measurements of intensity have been made for individual rotational lines of the atmospheric oxygen $b^1\sum_g^+(\upsilon'=0,2) \leftarrow X^3\sum_g^-(\upsilon''=0)$ or the A- and γ-bands by using different techniques such as: "White" multiple traversal absorption cells [38–40, 47–50], intracavity laser-absorption spectroscopy (ICLAS) [37], and cavity ring down spectroscopy (CRDS) [18, 51]. Previous measurements of the A-band absorption have been attempted to obtain experimental line parameters between 202 and 224 K. However, the temperatures had an uncertainty of 10 K, the actual spectra were not presented, and the temperature dependence of the pressure shift was not determined [50]. The sensitivity of CRDS [8, 52], phase-shift cavity ring down spectroscopy (PS-CRD) [6] and Fourier transform phase-shift cavity ring down spectroscopy [53] have been demonstrated by using several bands in the very weak forbidden $b^1\sum_g^+ \leftarrow X^3\sum_g^-$ transitions on gaseous molecular oxygen. Using the highly sensitive CRDS, the absorption spectra of the A-band of the $^{16}O^{18}O$, $^{16}O^{17}O$, $^{18}O_2$, $^{17}O^{18}O$ and $^{17}O_2$ and the γ-band of $^{16}O_2$, $^{16}O^{17}O$, $^{17}O_2$ and $^{18}O_2$ isotopomers of oxygen have been investigated [54, 55]. In addition, calculation of the atmospheric transmission function [38] and the magnetic dipole transition moment for the red atmospheric oxygen bands [56] have been made. Also, improved spectral parameters for those bands have been calculated and compared with HITRAN molecular absorption database [57].

The A-band plotted in Fig. 3 shows the shift in the distribution of rotational line intensity at the low temperatures with a maximum around $K''=3$ or 5 at 90 K. The room temperature spectrum shows a maximum around $K''=11$, with absorption bands visible up to $K''=25$. High K values disappear at lower temperatures. Quantitative measurements of the individual rotational line intensities of the oxygen A-band were not done because of the low spectral resolution. The intensity distribution of the simulated A-band in the two branches (not shown) was used to reproduce the intensity pattern of the experimental band and qualitatively confirm the temperature of the cell measured with the sensor attached to the optical cavity. Figure 4 shows the comparison between the experimental and simulated spectra of the γ-band at 90 K, respectively. The similarity between the rotational intensity distribution in the experimental spectra and the simulated spectra again qualitatively confirms the temperature measured in the cell. A quantitative confirmation of the low temperature was done by integrating the experimental rotational bands at 90 K.

The intensity of each rotational line in the oxygen γ-band is given by [37]

$$S(J'\upsilon' \leftarrow J''\upsilon'') = S(\upsilon' \leftarrow \upsilon'')\left(\frac{1}{Q(T)}\right) i_J \times \exp[-F_i hc/kT], \quad (7)$$

where $Q(T)$ is the rotational partition function, i_J is the Hönl-London factor, F_i is the energy of the lower state. Equation (7) assumes that the spectral range covered per each line is small [37]. Because the choice between the Hönl-London factors calculated by Watson or by Schlapp makes no significant difference [40], the Hönl-London factors of Schlapp were used and the factors (i_J) are $(1/2)(J''+1)$ for the ^PP branch and $(1/2)(J''+0.75)$ for the ^PQ branch. The observed values $S(J'\upsilon' \leftarrow J''\upsilon'')$ of the ^PP and ^PQ branches from $K''=1$ to $K''=11$ at 90 K were integrated according to

$$S(J'\upsilon' \leftarrow J''\upsilon'') = \left(\frac{1}{\rho}\right)\int \alpha(\nu)\, d\nu, \quad (8)$$

where $\alpha(\nu)$ in cm^{-1} is the wave number dependent absorption and ρ is the density in molecules/cm^3. Equation (7) can

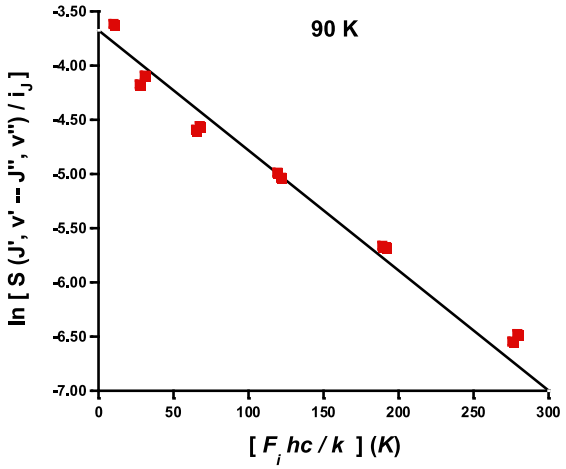

Fig. 5 Plot of (9) or $\ln(S(\upsilon' J' \leftarrow \upsilon'' J'')/i_J)$ vs. $F_i hc/k$. The slope is $(1/T)$. The straight line was obtained with points from the calculated spectrum at 90 K. The squares are from the observed spectrum

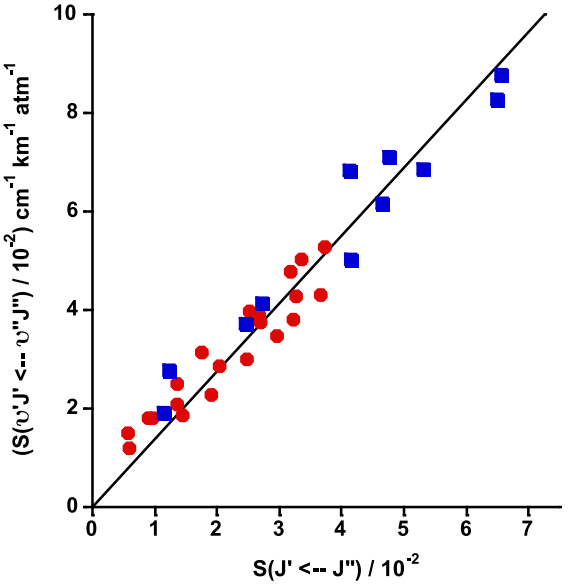

Fig. 6 Oxygen γ-band $S(\upsilon' J' \leftarrow \upsilon'' J'')$ (experimental) vs. $S(J' \leftarrow J'')$. The slope is $S(\upsilon' \leftarrow \upsilon'')$. Measurements at 295 K (●) and at 90 K (■)

be rewritten as

$$\ln\left(\frac{S(J'\upsilon' \leftarrow J''\upsilon'')}{i_J}\right) = \ln\left(\frac{S(\upsilon' \leftarrow \upsilon'')}{Q(T)}\right) - \frac{1}{T}\left(\frac{F_i hc}{k}\right) \tag{9}$$

where F_i values were calculated using equations from the reported values [37, 40] and the rotational partition function is given by $Q(T) = (3kT/B_e hc)$. The comparison is between the integrated observed and simulated absorptions. These values were plotted and are shown in Fig. 5. To facilitate the comparison, the straight line was obtained with the simulated spectrum (the points are not shown) at the known temperature. The squares are from the observed spectrum. The plot at 90 K shows the agreement between the calculated line and the experimental values.

Finally, the temperature independent $S(\upsilon' \leftarrow \upsilon'')$ was calculated. A plot of $S(J'\upsilon' \leftarrow J''\upsilon'')$ versus $S(J' \leftarrow J'') = (\frac{1}{Q(T)})i_J \exp[-F_i hc/kT]$ was obtained using the integrated absorptions at 297 and 90 K. The integrated values from (8) were calculated for three different densities or pressures (598, 495, and 384 Torr) at room temperature. The $S(J' \leftarrow J'')$ were also calculated for the ${}^P P$ and ${}^P Q$ lines of the γ-band. Also, a pressure series (181, 147, and 114 Torr) of the γ-band for oxygen were measured at 90 K. The $S(J'\upsilon' \leftarrow J''\upsilon'')$ values are the averages for the three different pressures at each temperature. The S values were in units of $\mathrm{cm^2\,cm^{-1}}$ molecules^{-1}. However, in the literature the vibrational band intensity is reported in units of $\mathrm{cm^{-1}\,km^{-1}\,atm^{-1}}$ at Standard Temperature and Pressure (STP). Each vibrational band intensity $S(J'\upsilon' \leftarrow J''\upsilon'')$ in units of ($\mathrm{cm^2\,cm^{-1}}$ molecule^{-1}) was multiplied by the factor: 2.6867×10^{24} $\mathrm{cm^{-2}}$ molecule $\mathrm{atm^{-1}\,km^{-1}}$ at (STP) [57] to make the conversion to $\mathrm{cm^{-1}\,km^{-1}\,atm^{-1}}$ (STP). These values were plotted together (295 and 90 K) and are shown in Fig. 6. The slope of the straight line that results is the vibrational band intensity $S(\upsilon' \leftarrow \upsilon'')$. The best fit of the straight line gives the vibrational band intensity $S(\upsilon' \leftarrow \upsilon'') = (1.37 \pm 0.08)$ $\mathrm{cm^{-1}\,km^{-1}\,atm^{-1}}$ (STP). For comparison, the $S(\upsilon' \leftarrow \upsilon'')$ values of the literature using different methods are: 1.50 [35], 1.26 ± 0.05 [37], 1.52 ± 0.07 [39], 1.22 [58], 1.31 [59], 1.52 [60]. All the literature values were obtained at room temperature. Our plot includes values at two temperatures 297 and 90 K. Altough our calculated value is in good agreement with the literature, a word of caution should be given. It is well known that when the resolution of the laser is of the same order of magnitude as the molecular bandwidth, it is not always possible to get the correct integrated band using CRD spectroscopy [18, 20] particularly when the intensities are weak. The vibrational cross section is the result of a linear least square average and this is probably the reason for the good agreement with the literature values. Some of our weak individual lines $S(J'\upsilon' \leftarrow J''\upsilon'')$ need to be corrected but this is out of the scope of this paper where the performance of the low temperature CRD cell and the use of off-axis alignment was the main focus.

The advantage of a long path cell operated at low temperatures is that is possible to simulate in the laboratory different planetary atmospheres. A typical case is the atmosphere of Titan, a satellite of Saturn, that has been reported to contain N_2 as the dominant gas, followed by CH_4 (1%) and C_2H_6, C_2H_2, C_2H_4, HCN, as well as C_3H_4, C_3H_8, C_4H_2, HC_3N, and C_2N_2. At 140, 40, and 10 Km of altitude, the atmospheric pressures are approximately 3, 152,

and 760 Torr and the temperatures are 140, 70, and 80 K, respectively [61]. A low temperature CRD optical cavity like the one described here, could provide laboratory data simulating conditions of pressure and temperature for Titan at different altitudes. The comparison and identification of absorption bands that occur in other satellites and planets of our solar system are also possible. For example, Neptune [62] shows the presence of H_2 , He (15%), CH_4, and C_2H_2 in a temperature range of 80–120 K. Uranus [63] shows H_2, He (15%), and CH_4 with an effective $T = 59$ K. Infrared observations of Jupiter [64] indicate the presence of H_2, CH_4, C_2H_2, C_2H_6 CH_3D, NH_3, PH_3, H_2O, and GeH_4, and He (11%) with atmospheric temperatures between 100–165 K.

Another application is related to the detection of atmospheric trace gases and their chemical reactions. The Earth's atmosphere is divided into regions on the basis of temperature gradients. In the lower atmosphere (troposphere) the air temperature falls with increasing altitude to reach a minimum of around 210 K between 10 and 16 km above sea level. The sensitivity of the cavity ring down technique is around 10^{13}–10^{11} molecules/cm^3 and it is possible to study in the laboratory the smallest concentrations of molecules such as NO_2, NO, NO_3, N_2O_5, O_3, HONO, and hydrocarbons simulating atmospheric conditions on Earth [65].

The observation of weakly bound complexes is possible with the low temperature CRD cell. Long path equilibrium cells have used Beer's law and Fourier transform infrared spectroscopy for studies of molecular complexes. The weak absorption features are enhanced by operation at low temperatures, high sample pressures, and enhanced path lengths obtained with a White cell. The equilibrium distributions in the cooled cell have facilitated thermodynamic studies of the binding energies of the complexes [66].

5 Conclusion

A low temperature cavity ring down technique was presented using phase shift and exponential decay to determine the time constant. Both CRD techniques perform well with this cell. In our experiment, the use of an off-axis alignment of the cavity: (1) increased the number of cavity modes, (2) increased the time efficiency of the laser beam coupling to the cavity, (3) increased de signal to noise ratio, (4) eliminated the need for piezoelectric modulation of the cavity length, and (5) eliminated the need for frequency dithering of the laser. This is very important because the cavity attached to a cryostat has to be isolated under vacuum. The rotational vibrational spectra for two different transitions of O_2 in the visible, the $(0 \leftarrow 0)$ and $(2 \leftarrow 0)$ bands of the $b^1\sum_g^+ \leftarrow X^3\sum_g^-$ transition a were obtained using CRD spectroscopy. The spectra were measured at 297 and 90 K and were reproduced using the PGOPHER program. Good agreement between the observed and calculated bands was obtained at 90 K giving a confirmation of the low temperature measured in the cell with temperature sensors. The temperature independent vibrational cross section calculated with integrated bands at two temperatures is in agreement with literature values. This CRD cell could be used to study weak absorptions of molecules relevant to planetary atmospheres and molecular complexes in equilibrium conditions.

Acknowledgements This work was supported by the Robert A. Welch Foundation under grant No. AA-1173. Partial support from the Baylor University Faculty Research Investment Program (FRIP) is also acknowledged. We thank Dr. C.M. Western for help with the simulation program.

References

1. Y. Perez-Delgado, C.E. Manzanares, J. Phys. Chem. A **114**, 7918 (2010)
2. Y. Perez-Delgado, E.K. Lewis, C.J. Moehnke, M.C. Salazar, A.J. Hernandez, C.E. Manzanares, Mol. Phys. **107**, 1367 (2009)
3. E.K. Lewis, C.J. Moehnke, J. Navea, C.E. Manzanares, Rev. Sci. Instrum. **77**, 073107 (2006)
4. C.J. Moehnke, E.K. Lewis, A. Lopez-Calvo, C.E. Manzanares, Chem. Phys. Lett. **418**, 576 (2006)
5. J.M. Herbelin, J.A. McKay, M.A. Kwok, R.H. Ueunten, D.S. Urevig, D.J. Spencer, D.J. Benard, Appl. Opt. **19**, 144 (1980)
6. R. Engeln, G. von Helden, G. Berden, G. Meijer, Chem. Phys. Lett. **262**, 105 (1996)
7. D.Z. Anderson, J.C. Frisch, C.S. Masser, Appl. Opt. **23**, 1238 (1984)
8. A. O'Keefe, D.A.G. Deacon, Rev. Sci. Instrum. **59**, 2544 (1988)
9. D. Romanini, K.K. Lehmann, J. Chem. Phys. **99**, 6287 (1993)
10. J. Morville, D. Romanini, A. Campargue, R. Bacis, Chem. Phys. Lett. **363**, 498 (2002)
11. M. Sneep, D. Ityaksov, I. Aben, H. Linnartz, W. Ubachs, J. Quant. Spectrosc. Radiat. Transf. **98**, 405 (2006)
12. J.U. White, J. Opt. Soc. Am. **32**, 285 (1942)
13. G. Herzberg, Astrophys. J. **115**, 337 (1952)
14. A. Watanabe, H.L. Welsh, Can. J. Phys. **45**, 820 (1965)
15. R.P. Blickensderfer, G.W. Ewing, R. Leonard, Appl. Opt. **7**, 2214 (1968)
16. R.W. McKellar, N. Rich, V. Soots, Appl. Opt. **9**, 222 (1970)
17. D. Horn, G. Pimentel, Appl. Opt. **10**, 1892 (1971)
18. J.H. van Helden, D.C. Schram, R. Engeln, Chem. Phys. Lett. **400**, 320 (2004)
19. J.B. Paul, L. Lapson, J.G. Anderson, Appl. Opt. **40**, 4904 (2001)
20. V.L. Kasyutich, P.A. Martin, Chem. Phys. Lett. **446**, 206 (2007)
21. J. Courtois, A.K. Mohamed, D. Romanini, Opt. Express **18**, 4845 (2010)
22. Y.A. Bakhirkin, A.A. Kosterev, C. Roller, R.F. Curl, F.K. Tittel, Appl. Opt. **43**, 2257 (2004)
23. D. Herriott, H. Kogelnik, R. Kompfner, Appl. Opt. **3**, 523 (1964)
24. V.L. Kasyutich, P.A. Martin, R.J. Holdsworth, Meas. Sci. Technol. **17**, 923 (2006)
25. V.L. Kasyutich, P.A. Martin, R.J. Holdsworth, Chem. Phys. Lett. **430**, 429 (2006)
26. F. Dong, M. Gupta, Sens. Actuators B **129**, 158 (2008)
27. J.D. Ayers, R.L. Apodaca, W.R. Simpson, D.S. Baer, Appl. Opt. **44**, 7239 (2005)
28. V.L. Kasyutich, C.E. Canosa-Mas, C. Pfrang, S. Vaughan, R.P. Wayne, Appl. Phys. B **75**, 755 (2002)

29. V.L. Kasyutich, C.S.E. Bale, C.E. Canosa-Mas, C. Pfrang, S. Vaughan, R. P Wayne, Appl. Phys. B **76**, 691 (2003)
30. V.L. Kasyutich, P.A. Martin, R. J Holdsworth, Appl. Phys. B **85**, 413 (2006)
31. D.S. Baer, J.B. Paul, M. Gupta, A. O'Keefe, Appl. Phys. B **75**, 261 (2002)
32. W. Zhao, X. Gao, W. Chen, W. Zhang, T. Huang, T. Wu, H. Cha, Appl. Phys. B **86**, 353 (2007)
33. G. Schuster, I. Labazan, J.N. Crowley, Atmos. Meas. Tech. **2**, 1 (2009)
34. G. Herzberg, *Molecular Spectra and Molecular Structure I. Spectra of Diatomic Molecules* (Van Nostrand, Princeton, 1950), p. 446
35. H.D. Babcock, L. Herzberg, Astrophys. J. **108**, 167 (1948)
36. J.K.G. Watson, Can. J. Phys. **46**, 1637 (1968)
37. M.A. Melieres, M. Chenevier, F. Stoeckel, J. Quant. Spectrosc. Radiat. Transf. **33**, 337 (1985)
38. T. Nakazawa, T. Yamanouchi, M. Tanaka, J. Quant. Spectrosc. Radiat. Transf. **27**, 615 (1982)
39. J.H. Miller, L.P. Giver, R.W. Boese, J. Quant. Spectrosc. Radiat. Transf. **16**, 595 (1976)
40. J.H. Miller, R.W. Boese, L.P. Giver, J. Quant. Spectrosc. Radiat. Transf. **9**, 1507 (1969)
41. PGOPHER, A Program for Simulating Rotational Structure, C.M. Western, University of Bristol. http://pgopher.chm.bris.ac.uk
42. National Institute of Standards and Technology NIST Chemistry web book. http://webbook.nist.gov/chemistry/
43. G.Y. Golubiatnikov, A.F. Krupnov, J. Mol. Spectrosc. **225**, 222 (2004)
44. G. Rouillé, G. Millot, R. Saint-Loup, H. Berger, J. Mol. Spectrosc. **154**, 372 (1992)
45. S. Brodersen, J. Bendtsen, J. Mol. Spectrosc. **219**, 248 (2003)
46. L.R. Zink, M. Mizushima, J. Mol. Spectrosc. **125**, 154 (1987)
47. B.E. Grossmann, C. Cahen, J.L. Lesne, J. Benard, G. Leboudec, Appl. Opt. **25**, 4261 (1986)
48. K.J. Ritter, T.D. Wilkerson, J. Mol. Spectrosc. **121**, 1 (1987)
49. A.J. Phillips, F. Peters, P.A. Hamilton, J. Mol. Spectrosc. **184**, 162 (1997)
50. L.R. Brown, C. Plymate, J. Mol. Spectrosc. **199**, 166 (2000)
51. S. Xu, D. Dai, J. Xie, G. Sha, C. Zhang, Chem. Phys. Lett. **303**, 171 (1999)
52. A. Teslja, P.J. Dagdigian, Chem. Phys. Lett. **400**, 374 (2004)
53. E. Hamers, D. Schram, R. Engeln, Chem. Phys. Lett. **365**, 237 (2002)
54. H. Naus, A. de Lange, W. Ubachs, Phys. Rev. A **56**, 4755 (1997)
55. H. Naus, K. Navaian, W. Ubachs, Spectrochim. Acta A **55**, 1255 (1999)
56. B. Minaev, O. Vahtras, H. Agren, Chem. Phys. **208**, 299 (1996)
57. R.R. Gamache, A. Goldman, L.S. Rothman, J. Quant. Spectrosc. Radiat. Transf. **59**, 495 (1998)
58. C.W. Allen, Astrophys. J. **85**, I56 (1937)
59. H.C. van de Hulst, Ann. D' Astrophys. **8**, 12 (1945)
60. M. Mizushima, S. Yamamoto, J. Mol. Spectrosc. **148**, 447 (1991)
61. C.M. Anderson, R.E. Samuelson, Icarus **212**, 762 (2011)
62. B. Conrath, F.M. Flasar, R. Hanel, V. Kunde, W. Maguire, J. Pearl, J. Pirraglia, R. Samuelson, P. Gierasch, A. Weir, B. Bezard, D. Gautier, D. Cruikshank, L. Horn, R. Springer, W. Shaffer, Science **246**, 1454 (1989)
63. R. Hanel, B. Conrath, F.M. Flasar, V. Kunde, W. Maguire, J. Pearl, J. Pirraglia, R. Samuelson, D. Cruikshank, D. Gautier, P. Gierasch, L. Horn, P. Schulte, Science **233**, 70 (1986)
64. R. Hanel, B. Conrath, M. Flasar, L. Herath, V. Kunde, P. Lowman, W. Maguire, J. Pearl, J. Pirraglia, R. Samuelson, D. Gautier, P. Gierasch, L. Horn, S. Kumar, C. Ponnamperuma, Science **206**, 952 (1979)
65. D.B. Atkinson, Analyst **128**, 117 (2003)
66. A.R.W. McKellar, Faraday Discuss. **97**, 69 (1994)